



Fluid Dynamics and Transport Phenomena

Drag-induced breakup mechanism for droplet generation in dripping within flow focusing microfluidics[☆]



Ping Wu¹, Zhaofeng Luo², Zhifeng Liu¹, Zida Li¹, Chi Chen³, Lili Feng¹, Liquan He^{1,*}

¹ Department of Thermal Science and Energy Engineering, University of Science and Technology of China, Hefei, 230027, China

² School of Life Sciences, University of Science and Technology of China, Hefei 230027, China

³ Department of Mechanical Engineering, Hong Kong University of Science and Technology, Hong Kong, China

ARTICLE INFO

Article history:

Received 2 March 2013

Received in revised form 11 June 2013

Accepted 22 November 2013

Available online 2 October 2014

Keywords:

Microfluidics

Droplet

Dripping

Flow focusing

Thread

Force balance

ABSTRACT

Based on viscous drag-induced breakup mechanism, a simple model was proposed to predict the dripping droplet size as a function of controllable parameters in flow focusing micro devices. The size of thread before breakup was also investigated through laminar flow theory. Experiments and numerical simulations by VOF are carried out simultaneously to validate the theoretical analysis, showing that droplet size decreases rapidly with the increase of the flow rate ratio and capillary number.

© 2014 The Chemical Industry and Engineering Society of China, and Chemical Industry Press. All rights reserved.

1. Introduction

Micro droplets provide versatile ways for chemical and biological analysis such as multiple emulsion [1], polymerase chain reaction (PCR) [2–5], drug delivery [6–8], microreactors [9,10] and so on. Most of these applications demand highly uniform droplets in size, and flow-focusing microfluidic device is one of the most widely utilized method for such droplet formation. In these microchannels there are usually two immiscible fluids such as water and oil, and the inner liquid is squeezed to form a thread along the centerline by wrapping viscous oil. The thread head will become unstable when flowing through an orifice and releases monodisperse droplets by spontaneous generation. A lot of work have been carried out [11–14] since this approach was first implemented by Anna *et al.* [15], and experiments have shown that fluid flow undergoes several distinct flow regimes including jetting and dripping as the capillary number alters [16,17]. In the jetting pattern, the water thread will be extended to a long distance out of the orifice, and the thread is subjected to the well-known Rayleigh–Plateau capillary instability that is dominantly responsible for droplet

formation. As for the dripping pattern, the thread will experience a sudden expansion near the exit of orifice, causing velocity redistribution and pressure drop in the flow field, and the detailed breakup mechanism appears more complicated and remains controversial to date. Several researches believed that the capillary instability also plays important role in droplet breakup in dripping, and they speculated that droplet radius should be proportional to the thread size [16,18]. However, other investigations suggested that the droplet/bubble pinch-off period in dripping is weakly dependent on interfacial tension and thus it is difficult to solely associate the droplet/bubble rupture process with capillary instability as expected [11,19–24]. In general, the dripping regime produces more homogeneous droplets than that of jetting regime, and no simple theoretical model was yet reported to explain the collapse mechanism and predict the droplet size distribution [25].

This paper attempts to present an intuitive force-balance model to elucidate the droplet breakup mechanism in dripping mode and forecast the droplet size as a function of flow conditions. Numerical investigation suggests that viscous drag contributes appreciably in droplet detachment at extremely low Reynolds and Weber numbers [26]. From this standpoint, we describe and calculate holding and detaching forces acting on a growing droplet, and show that the dynamical competition between them determines the droplet deformation and breakup, as well as the final droplet size. Experiments and numerical simulations are carried out simultaneously to validate our theoretical analysis.

[☆] Supported by the National Natural Science Foundation of China (50876100) and the Grade A Technology Development Foundation of USTC (ZC9850340103).

* Corresponding author.

E-mail address: heliquan@ustc.edu.cn (L. He).

2. Model Development

2.1. Drag-induced droplet breakup mechanism

In our flow focusing microfluidic device shown in Fig. 1(a), water and oil act as inner and outer phases. With the net action of oil on water, the liquid–liquid interface is squeezed strongly towards the center line and water forms a thread in the entrance of the orifice. In dripping regime, the thread expands abruptly at the very exit of the nozzle, and interfacial tension forces the thread head into spherical shape. However, the spherical droplet is easily confined into disk-like ones when the droplet size grows larger than channel depth, as shown in Fig. 1(b). The sudden expansion leads to deceleration and stagnation of the spherical tip, and viscous drag from outer fluid acting analogously as those co-flowing capillary drop-formation devices is a main detaching force. At low Reynolds number, viscous drag on the emerging droplet stretches and thins the neck, and becomes more important than capillary instability in the role of droplet breakup.

We now propose a relatively simple hydrodynamic model to explain the droplet detachment when only one droplet is in birth at the dripping thread head. As illustrated in Fig. 1(a), R_{drop} is droplet radius, and the shape of water jet flow in orifice region is close to cylindrical with a diameter d_j . In the growth of a droplet, forces acting on the growing droplet volume τ can be divided into holding and detaching ones. During the expansion, the interfacial tension F_σ acting around thread surface is a resistance preventing the droplet expanding and detaching. In the presence of the neck connecting the droplet, the droplet shape of it is not entirely spherical, leading to the fact that the net effect interfacial tension acting on the growing droplet is opposite to the flow direction and can be perceived as a body force principally preventing the drop neck breakup. In contrast, the Stokes-like force F_S consisting of viscous and pressure stress performs as the most principal drag impelling the thread breakup. The linear momentum force F_L caused by inner fluid momentum is also considered as detaching forces accelerating the breakup. Generally, the inertial force is always negligible since it is about 10^{-4} – 10^{-7} order of magnitude less than others in these low Reynolds number microfluidics ($Re \approx 0.001$ – 0.5). In the beginning, interfacial tension plays a dominate role and holds the droplet as a slender tube [27]. With the growth of droplet, detaching forces become more important. When these detaching forces achieve balance with the holding one, the forming droplet begins to break away from the thread and tends to develop as spherical shape by the interfacial tension. This drag-induced breakup mechanism performs analogously to the breakup of a pendant drop under gravitational force.

2.2. Force balance model

Based on the above statement, one can write the force balance equation to determine the critical condition of droplet detachment as

$$F_\sigma = F_S + F_L. \quad (1)$$

Interfacial tension is generally described as

$$F_\sigma = \pi d_j \sigma. \quad (2)$$

Here the cylindrical thread holds the drop, and σ is the interfacial tension coefficient.

Before detachment the droplet bears viscous drag increasingly from the outer fluid and it can be approximately calculated according to Stokes' Law at low Reynolds number. We must realize that the growing droplet is easily confined to disk-like ones due to a high width-to-depth ratio of the channel, and the fluid flow in microfluidics is always simplified as a planar flow. Nevertheless, the disk-like droplets would transit into spherical ones as the flow rate ratio ($q = Q_o/Q_w$) increases, resulting in those droplets whose size is even smaller than the channel depth. Our experiments confirm that spherical droplets are generated when q is higher than 30. So we describe the viscous drag according to a disk-like (2D) or spherical (3D) droplet, which is approximately determined by flow rate ratio. In addition, the internal circulation flow within micro droplets can be always neglected owing to the use of surfactant, and the Stokes flow assumption is acceptable in both cases.

In 2D case, the disk-like droplets with a depth h is considered as a cylinder and we obtain the viscous drag of per unit length on the grounds of the unbounded Oseen flow around a two-dimensional cylinder as [28]:

$$F_{S1,\infty} = \frac{4\pi\mu_o V_o}{\ln 3.703 - \ln Re}. \quad (3)$$

With the consideration of microchannel wall effect, the net Stokes drag acting on a growing droplet can be described according to the Brenner's study [29] as

$$F_{S1} = \frac{F_{S1,\infty} h}{1 - \beta F_{S1,\infty} h / 6\pi\mu_o V_o l + O\left[\left(R_{\text{drop}}/l\right)^3\right]} \approx \frac{F_{S1,\infty} h}{1 - \beta F_{S1,\infty} h / 6\pi\mu_o V_o l}. \quad (4)$$

Here, $V_o = 2Q_o/(w_{\text{down}}h)$, $l = w_{\text{down}}/2$, and β is a constant referring to the shape factors, $\beta = 1.004$ is always appropriate for the case of parallel plate flow with an obstacle in the center line [29].

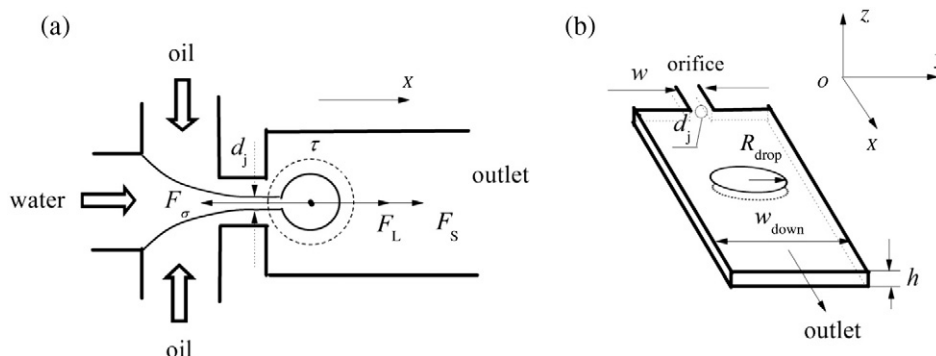


Fig. 1. (a) Droplet formation in flow focusing micro geometry and forces acting on a growing droplet τ ; (b) illustration of a disk-like droplet confined between the top and bottom wall.

In the 3D case, the classical Stokes drag acting on a spherical droplet is

$$F_{S2,\infty} = 6\pi\mu_o V_o R_{\text{drop}}. \quad (5)$$

Likewise, the net Stokes drag is calculated with wall effect considered [29],

$$F_{S2} = \frac{F_{S2,\infty}}{1 - \beta F_{S2,\infty}/6\pi\mu_o V_o l + O\left[\left(R_{\text{drop}}/l\right)^3\right]} \approx \frac{F_{S2,\infty}}{1 - \beta F_{S2,\infty}/6\pi\mu_o V_o l}. \quad (6)$$

Thus the viscous drag is determined by flow rate ratio as

$$F_S = \begin{cases} F_{S1}, & 1 < q < 30, \text{ disk-like} \\ F_{S2}, & q > 30, \text{ spherical} \end{cases}. \quad (7)$$

The effect of the inner fluid momentum crossing the boundaries can be regarded as linear momentum force approximately described as [30]

$$F_L = \rho_w Q_w V_w. \quad (8)$$

Similar to co-flowing, we define a capillary number characterizing the relative importance of viscous stresses and capillary pressure across the interface between the two phases as

$$Ca = \frac{\mu_o u_o}{\sigma} = \frac{\mu_o Q_o}{\sigma(wh - \pi d_j^2/4)}. \quad (9)$$

Ultimately, we obtain the prediction of final droplet size through Eqs. (1)–(7):

$$R_{\text{drop}} = \begin{cases} \frac{3.703\mu_o w_{\text{down}} h}{4\rho_o Q_o} e^{-\frac{4}{3w_{\text{down}}}[6\mu_o Q_o \pi^2 d_j^2 / (\pi^2 d_j^2 \sigma - 4\rho_w Q_w^2) + \beta h]}, & (R_{\text{drop}} > h, 1 < q < 30) \\ \frac{w_{\text{down}} h (\pi^2 d_j^2 \sigma - 4\rho_w Q_w^2)}{6\pi^2 \mu_o Q_o d_j^2 + 2\beta h (\pi^2 d_j^2 \sigma - 4\rho_w Q_w^2)}, & (R_{\text{drop}} < h, q > 30) \end{cases}. \quad (10)$$

2.3. Thread size

Eqs. (2) and (10) indicate that d_j must be calculated out first when estimating the interfacial tension force. Unlike the calculation of viscous drag as planar flow, the interfacial tension force is calculated according to three-dimensional (3D) flow case because the thread size is always smaller than the width and depth of orifice, especially in dripping regime (shown in Fig. 4(a)). It is meaningful that the thread shape would always keep cylindrical in the rectangular cross-section of orifice region and 3D fluid flow is more reasonable in the calculation of the thread size.

It is observed that the radius of water thread R_{jet} ($R_{\text{jet}} = d_j/2$) thins slightly just before achieving the force balance in the orifice region, and is determined mainly by flow rate ratio [16,18]. The shape of inner fluid in the rectangular orifice region is close to cylindrical, and the assumption of fully developed inner flow is adopted. However, the forward movement of water–oil interface makes the velocity boundary condition little different from the conventional pipe flow. We prove in the 2D flow case (seen in Appendix) that the parabolic velocity profile of inner fluid should be modified by adding a constant, which equals the interface velocity between two liquid. The present velocity profile is coincident with the prediction of Utada *et al.* [16], and matches the viscous shear stress across the interface. Extrapolated to 3D case, the water velocity is written as

$$u_w(r) = \frac{1}{4\mu_w} \left(-\frac{dp}{dx} \right)_w (R_{\text{jet}}^2 - r^2) + \bar{V} \quad (11)$$

where $r = \sqrt{y^2 + z^2} \leq R_{\text{jet}}$, \bar{V} denotes the average velocity at the cylindrical interface determined by

$$\bar{V} = \frac{1}{2\pi R_{\text{jet}}} \int_L u_o(y, z) ds \quad (12)$$

where the integral curve $L: y^2 + z^2 = R_{\text{jet}}^2$, u_o is the oil velocity distribution obtained from the traditional Poiseuille flow in rectangular pipe [31],

$$u_o(y, z) = \frac{1}{2\mu_o} \left(-\frac{dp}{dx} \right)_o \times \left[w^2 - z^2 + \frac{32w^2}{\pi^3} \sum_{n=0}^{\infty} \frac{(-1)^n \cosh\left(\frac{2n+1}{2w}\pi y\right) \cos\left(\frac{2n+1}{2w}\pi z\right)}{(2n+1)^3 \cosh\left(\frac{2n+1}{2w}\pi h\right)} \right] \quad (13)$$

We reach the conclusion that the first term of the infinite series in the expression above was far more dominant than the others and the relative tolerance between Eq. (13) and Eq. (14) below is $O(10^{-5})$. For $n = 0$, then

$$u_o(y, z) = \frac{1}{2\mu_o} \left(-\frac{dp}{dx} \right)_o \times \left[w^2 - z^2 + \frac{32w^2 \cosh\left(\frac{\pi y}{2w}\right) \cos\left(\frac{\pi z}{2w}\right)}{\pi^3 \cosh\left(\frac{\pi h}{2w}\right)} \right] \quad (14)$$

where w and h denote respectively to the width and depth of the orifice channel shown in Fig. 1(b). Since the cylindrical thread size is constant through the orifice, the pressure difference caused by interfacial tension between two phases is also nearly invariable, suggesting that the pressure gradient of two phases equals each other. After the simplification, a lot of work can be relieved in the integration for calculating the thread size with sufficient accuracy. Thereupon, R_{jet} is also calculated through the given inlet flow rate ratio as

$$q = \frac{4 \left(\int_{\frac{h}{2}-R_{\text{jet}}}^{\frac{h}{2}} \int_0^{\frac{w}{2}} u_o(y, z) dy dz + \int_0^{R_{\text{jet}}} \int_{\frac{h}{2}-R_{\text{jet}}}^{\frac{h}{2}} u_o(y, z) dz dy \right)}{\int_0^{R_{\text{jet}}} u_w(r) 2\pi r dr}. \quad (15)$$

In Section 5.2 we will give a reasonable simplified expression for the calculation of thread size through numerical approximation from Eq. (15).

Now we can summarize that the flow rate ratio determines the thread size, and the final droplet size can be estimated from the force balance breakup mechanism described as Eq. (1). The prediction is obtained entirely from the inlet parameter, fluid material properties and channel size but not scaling relation.

3. Numerical Simulation

3.1. The VOF method

To confirm the model above and acquire more detail of the breakup mechanism, numerical simulation is carried out. Volume of Fluid (VOF) method is one of the most powerful models to track the motion of interface in multiphase [32–36].

The simulation is implemented in FLUENT 6.3.26. Here we define oil and water as primary and second phases, and the variable α refers to the volume fraction of second phase added to global equation. Volume fraction is calculated by

$$\frac{\partial \alpha}{\partial t} + \mathbf{V} \cdot \nabla \alpha = \frac{S_\alpha}{\rho_w}. \quad (16)$$

Generally, the source term S_α does not exist in our case. The advection of the volume equation relies on the flow field, and the revised momentum equation with surface tension as a body force is expressed as

$$\frac{\partial}{\partial t}(\rho \mathbf{V}) + \nabla \cdot (\rho \mathbf{V} \mathbf{V}) = -\nabla p + \nabla \cdot [\mu \nabla \mathbf{V} + \nabla \mathbf{V}^T] + \rho \mathbf{g} + \mathbf{F}. \quad (17)$$

Density and viscosity in each cell are calculated as the following averages:

$$\rho = \alpha \rho_w + (1-\alpha) \rho_o \quad (18)$$

$$\mu = \alpha \mu_w + (1-\alpha) \mu_o. \quad (19)$$

Due to Brackbill's contribution [37,38], surface tension force can be added in momentum equation as a body force:

$$\mathbf{F} = \frac{2\sigma \kappa \rho \nabla \alpha}{\rho_w + \rho_o} \quad (20)$$

where the curvature of the interface κ can be defined as

$$\kappa = \nabla \cdot \mathbf{n} \quad (21)$$

$$\mathbf{n} = \frac{\nabla \alpha}{|\nabla \alpha|}. \quad (22)$$

Discretization of flow equation is by a second order upwind format with mesh element generated as $1 \mu\text{m}$. To stabilize the iteration, we set a small fixed time-step as $0.1 \mu\text{s}$ initially. After hundreds of iterations, we increase the time-step slightly. The Courant number is defined in VOF model as

$$Co = \frac{\Delta t}{\Delta x_{\text{cell}}/v_{\text{fluid}}}. \quad (23)$$

We set the global maximum Courant number to 0.5 to accelerate the convergence rate while maintaining the accuracy of calculation.

Near the interface, geometric reconstruction scheme is adopted to obtain more accurate interface shape. FLUENT provides standard geometric reconstruction scheme to implement the interpolation near the

fluid–fluid interface using a piecewise-linear approach. The first step in this reconstruction scheme is calculating the position of the linear interface relative to the center of each partially-filled cell, based on the information about the volume fraction and its derivatives in both directions. The second step is calculating the advecting amount of fluid through each face using the computed linear interface representation and information about the normal and tangential velocity distribution on the face. The third step is calculating the volume fraction in each cell using the balance of fluxes calculated during the previous step.

3.2. The importance of meshes

The computational results, especially the accuracy of the interface shape and curvature, are directly affected by the grids. To find out the most appropriate size of the elements, four cases of 2D simulation with different mesh sizes ($\Delta x = 10 \mu\text{m}$, $4 \mu\text{m}$, $2 \mu\text{m}$ and $1 \mu\text{m}$) are conducted as shown in Fig. 2. It suggests that the coarsest grid produces laminar stratified flow of oil–water–oil rather than droplets. Though droplet generation can be observed in the case of $\Delta x = 4 \mu\text{m}$, the interface shape obtained in the upstream of the orifice is chaotic and it is illogical with polydisperse droplets instead of monodisperse ones. When the element size is $1 \mu\text{m}$ the perfect results as well as the independence of grid are achieved. Therefore all the subsequent simulations are conducted on the grids with $\Delta x = 1 \mu\text{m}$.

Results of the simulations make the process of focusing and breakup plainly visualized, and the size of thread and droplet can be calculated from volume fraction distribution of second phase. Flow parameters, material property and channel geometry is conveniently adjustable, with various droplet size acquired to validate the theoretical analysis.

4. Experimental Approach

Flow focusing microfluidic chips are fabricated *via* soft-lithography and replica molding [39] to demonstrate droplet formation. Polydimethylsiloxane (PDMS) and its curing agent (SYLGARD® 184, Dow Corning, Michigan USA) is fully mixed with a mass ratio of 10:1, and then poured on a monolayer mold made by SU-8 Resists (MicroChem Corp., USA) over a silicon wafer. The polymer is peeled off after baked for 1 h under 90°C , exposed to UV-light for 3 h, and then immediately bonded to a smooth PDMS face. All the depth of microchannel is $h =$

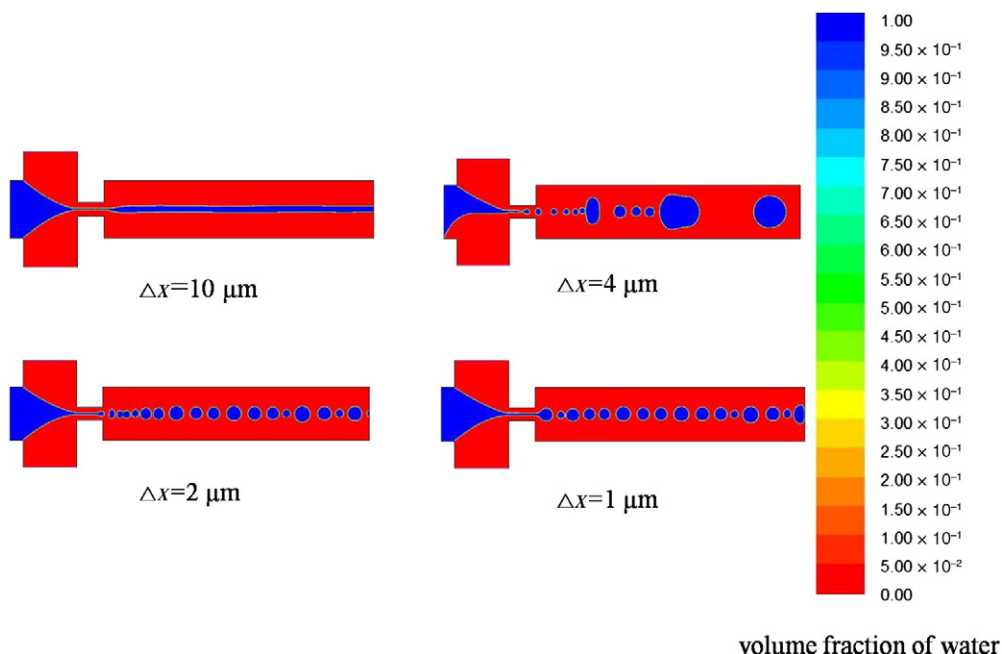


Fig. 2. Test of the independence of simulation on grids ($\rho_o = 980 \text{ kg} \cdot \text{m}^{-3}$, $\rho_w = 1000 \text{ kg} \cdot \text{m}^{-3}$, $\mu_o = 0.048 \text{ Pa} \cdot \text{s}$, $\mu_w = 0.001 \text{ Pa} \cdot \text{s}$, $\sigma = 0.023 \text{ N} \cdot \text{m}^{-1}$, $Q_w = 2 \mu\text{l} \cdot \text{h}^{-1}$, $Q_o = 20 \mu\text{l} \cdot \text{h}^{-1}$).

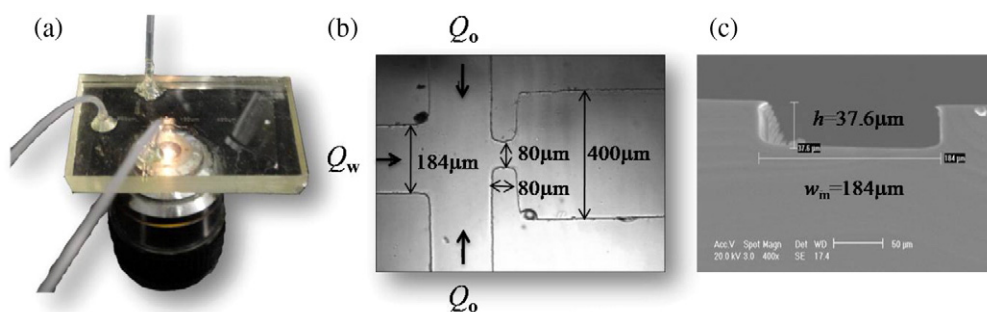


Fig. 3. (a) Microfluidic chip in experiments. (b) Detailed size of flow-focusing microchannel in vertical view. (c) Image of the channel cross-section in scanning electron microscopy (SEM).

37.6 μm and the width of inlet channel is $w_{\text{in}} = 184 \mu\text{m}$. Two widths of the channel orifice ($w = 80, 100 \mu\text{m}$) with different outlets ($w_{\text{down}} = 200, 400 \mu\text{m}$) are used in the experiments.

As illustrated in Fig. 3, mineral or silicon oil is used as the continuous liquid and injected into the channel through lateral inlets by a syringe pump (New Era Pump Systems Inc. USA), while deionized

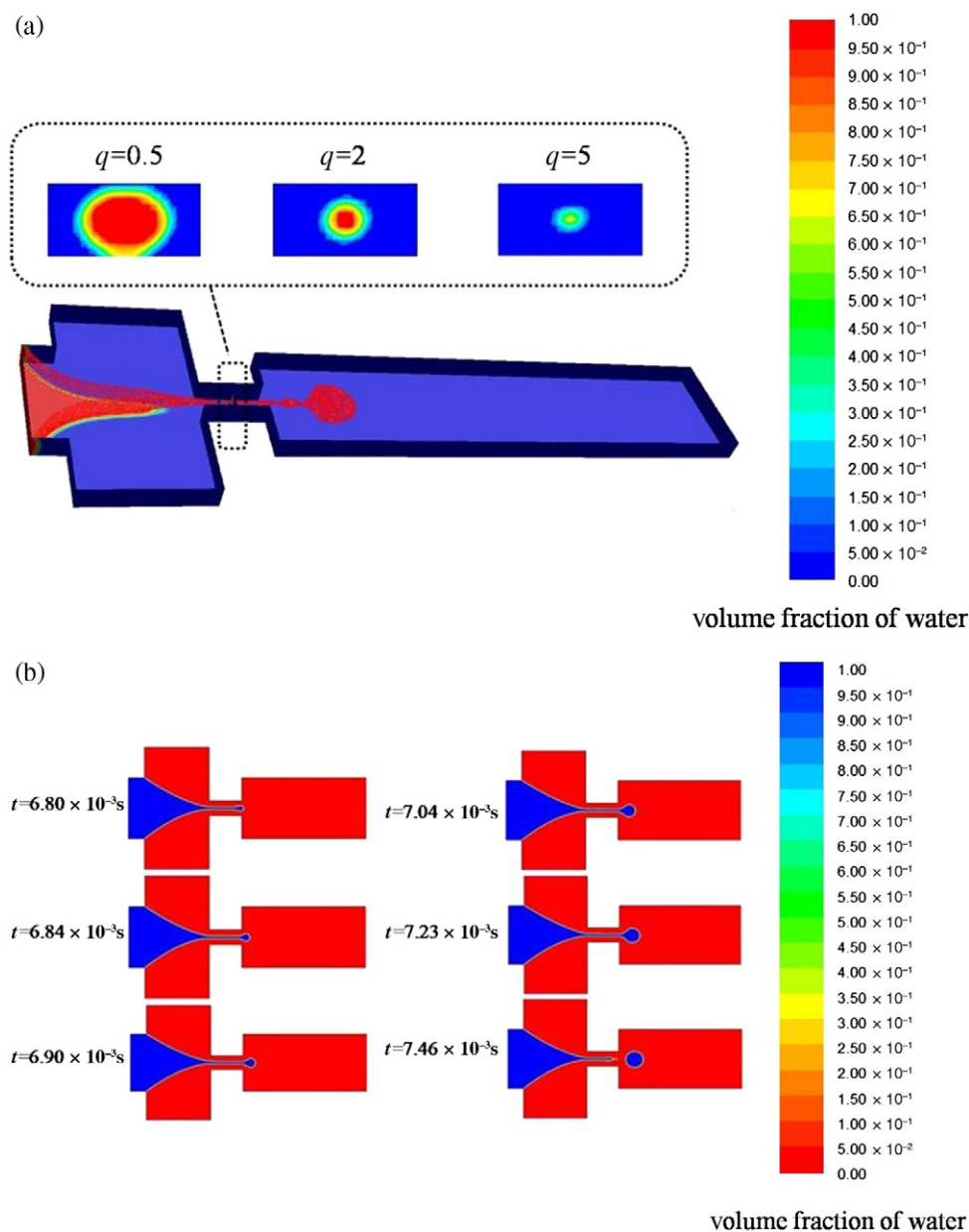


Fig. 4. Dispersed phase distribution in the cross-section perpendicular to the direction of flow in the orifice region. ($\rho_o = 980 \text{ kg} \cdot \text{m}^{-3}$, $\rho_w = 1000 \text{ kg} \cdot \text{m}^{-3}$, $\mu_o = 0.048 \text{ Pa} \cdot \text{s}$, $\mu_w = 0.001 \text{ Pa} \cdot \text{s}$, $\sigma = 0.023 \text{ N} \cdot \text{m}^{-1}$, $Q_w = 2 \mu\text{l} \cdot \text{h}^{-1}$). (b) Horizontal cross-section view of simulation results of the detailed droplet breakup process. ($q = 5$, $Q_w = 2 \mu\text{l} \cdot \text{h}^{-1}$, $\mu_o = 0.048 \text{ Pa} \cdot \text{s}$, $\mu_w = 0.001 \text{ Pa} \cdot \text{s}$, $\rho_o = 980 \text{ kg} \cdot \text{m}^{-3}$, $\rho_w = 1000 \text{ kg} \cdot \text{m}^{-3}$, $\sigma = 0.023 \text{ N} \cdot \text{m}^{-1}$).

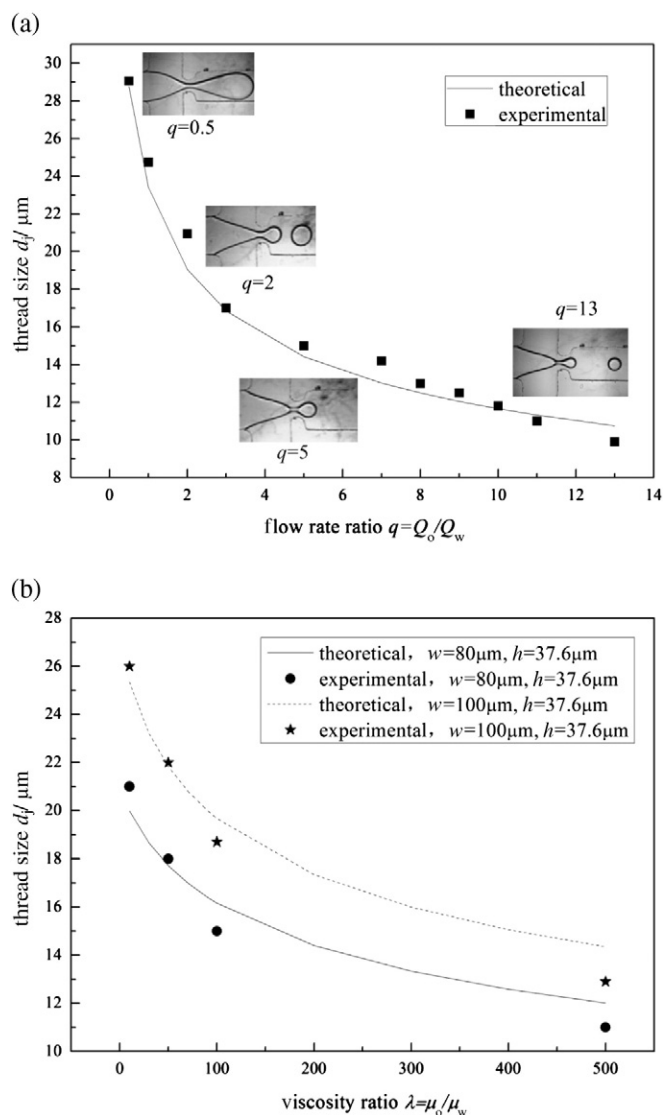


Fig. 5. (a) Theoretical and experimental thread size versus flow rate ratio. ($\rho_o = 980 \text{ kg}\cdot\text{m}^{-3}$, $\rho_w = 1000 \text{ kg}\cdot\text{m}^{-3}$, $\mu_o = 0.048 \text{ Pa}\cdot\text{s}$, $\mu_w = 0.001 \text{ Pa}\cdot\text{s}$, $\sigma = 0.023 \text{ N}\cdot\text{m}^{-1}$, $Q_w = 10 \mu\text{l}\cdot\text{h}^{-1}$). (b) Theoretical and experimental thread size versus viscosity ratio and orifice size. ($\rho_o = 980 \text{ kg}\cdot\text{m}^{-3}$, $\rho_w = 1000 \text{ kg}\cdot\text{m}^{-3}$, $\mu_w = 0.001 \text{ Pa}\cdot\text{s}$, flow rate ratio $q = 5$, $Q_w = 2 \mu\text{l}\cdot\text{h}^{-1}$, w and h denote the width and depth of the orifice).

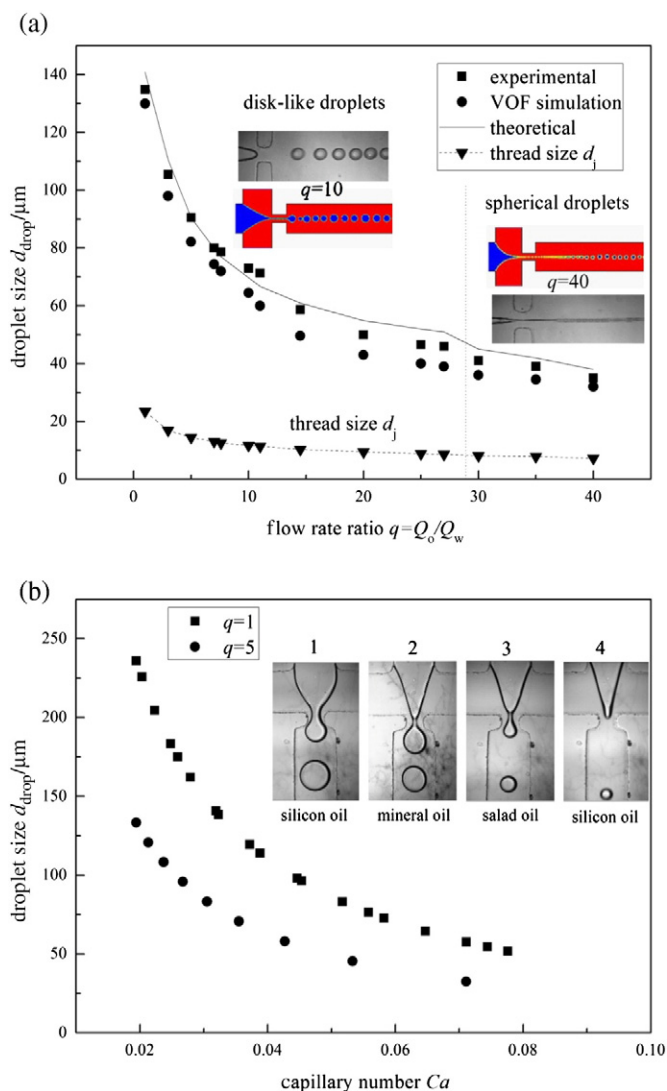


Fig. 6. (a) Droplet diameter versus flow rate ratio. ($\rho_o = 980 \text{ kg}\cdot\text{m}^{-3}$, $\rho_w = 1000 \text{ kg}\cdot\text{m}^{-3}$, $\mu_o = 0.048 \text{ Pa}\cdot\text{s}$, $\mu_w = 0.001 \text{ Pa}\cdot\text{s}$, $\sigma = 0.023 \text{ N}\cdot\text{m}^{-1}$, $Q_w = 2 \mu\text{l}\cdot\text{h}^{-1}$). (b) Theoretical droplet size versus capillary number. For silicon oil 1, $q = 1$, $\mu_o = 0.01 \text{ Pa}\cdot\text{s}$, $\sigma = 0.0115 \text{ N}\cdot\text{m}^{-1}$, $Ca = 0.01$; for mineral oil 2, $q = 5$, $\mu_o = 0.048 \text{ Pa}\cdot\text{s}$, $\sigma = 0.023 \text{ N}\cdot\text{m}^{-1}$, $Ca = 0.02$; for salad oil 3, $q = 5$, $\mu_o = 0.098 \text{ Pa}\cdot\text{s}$, $\sigma = 0.0269 \text{ N}\cdot\text{m}^{-1}$, $Ca = 0.03$; for silicon oil 4, $q = 10$, $\mu_o = 0.5 \text{ Pa}\cdot\text{s}$, $\sigma = 0.0461 \text{ N}\cdot\text{m}^{-1}$, $Ca = 0.052$.

water acting as the disperse phase, is transfused through the central inlet. Q_o and Q_w are the inlet flow rate of oil and water, respectively. Dripping regime is observed through an optic microscope by a CCD camera throughout the experiments by controlling the flow rate ratio q ranging from 1 to 40. Different droplet sizes are reported and compared with those of theoretical and simulation results.

5. Results and Discussion

5.1. Simulated breakup process of droplet formation

In the VOF simulation, we firstly monitor the phase distribution in the cross-section of orifice to explore the shape of the thread shown in Fig. 4(a). It is strongly validated that cylindrical-shape thread is acceptable when the flow rate ratio is higher than 1 in dripping regime. Furthermore, we show the detailed viscous drag-induced breakup process in numerical

simulation as Fig. 4(b), where we can see that the drop begins to develop near the orifice exit, and the thread size is almost invariable before the droplet detaches. The result is in good agreement with the assumption in theoretical calculation of thread size.

5.2. Thread size

Fig. 5(a) presents the results of prediction and experiments of thread size. High oil–water flow rate ratio means inner fluid would occupy less volume proportion in orifice resulting in more slender thread. It indicates as in the theoretical analysis that the larger the thread size, the stronger the holding interfacial tension force, and the harder the detachment resulting in larger droplets. Plugging droplets are generated when the oil flow rate is lower than that of water, and dripping occurs more obviously when $q > 1$. The careful measurement data validated the theoretical result from Eq. (15) about thread size. Fig. 5(b) shows the effect

of viscosity ratio and orifice size, and it is found that the thread size decreases rapidly with the increase of viscosity ratio and the narrowing of orifice. The viscosity difference between two phases causes the inner fluid to develop a different velocity profile from that of the outer fluid, and it exerts influence on the flow rate ratio determining the final thread size.

Since the flow rate ratio q , viscosity ratio λ and orifice size contribute appreciably on thread size according to the results of Figs. 5(a) and (b), we can give a rational expression about thread size as

$$\frac{\pi d_j^2}{4wh} = \frac{A}{1 + q + q\sqrt{1 + 1/(q\lambda)}}. \quad (24)$$

Numerical calculation gives the constant $A = 1.301$, and Eq. (24) has sufficient precision for estimating the value of d_j .

5.3. Prediction of droplet size

The force balance model above explained that droplets would pinch off when detaching effect surmount the holding force around the spherical interface. The prediction of droplet size versus flow ratio from Eq. (10) is also in good agreement with both numerical simulation and experiments as shown in Fig. 6(a). As mentioned above, larger thread size leads to stronger interfacial tension and longer detachment time with bigger droplets achieved. Furthermore, one can observe that the dripping will perform tempestuously as flow ratio increases over 30 with tinier spherical droplets generated, yet the homogeneity of the size would not be guaranteed. We believe that drag-induced breakup mechanism would give way to capillary instability in higher flow rate, and jetting regime occurs when droplet size is so close to the thread.

Fig. 6(b) plots the theoretical droplet size versus capillary number, and the curve tendency is coincident with those previous researches [24]. Larger capillary number means the droplet would bear more viscous drag, resulting in shorter time to achieve the force balance for collapse and smaller size. In the corresponding experiments we use four different oils as continuous phase (silicon oil with lower and higher viscosity, mineral oil and salad oil) and adjust the flow rate to obtain different capillary numbers to explore its effect. Results of experimental images in the inset of Fig. 6(b) confirm that the droplet size decreases with the increase of capillary number.

6. Conclusions

By virtue of viscous drag-induced breakup mechanism, a simple model is proposed to predict the droplet size as a function of controllable parameters. The droplet breakup is explained in light of hydrodynamics at low Reynolds number and the integral momentum equation. Limitations exists in the model such as it fails in the instability-dominate breakup jetting regime at the highest flow rate, but results of the final droplet size prediction is still in remarkable agreement with the experimental measurements and numerical simulations, suggesting that higher flow rate ratio and capillary number will generate finer emulsion droplets in dripping regimes. This theoretical analysis shows that droplet size in flow focusing microfluidics is predictable and controllable, which is meaningful for the control of droplet formation, operating condition selection and the microfluidic geometry excogitation.

Nomenclature

Ca	capillary number ($=\mu_o u_o/\sigma$)
Co	Courant number ($=v_{\text{fluid}} \Delta t/\Delta x$)
d_j	thread diameter, μm
F_L	linear momentum force, N
F_S	Stokes-like force, N
F_σ	interfacial tension, N
h	channel depth, μm
l	half width of the downstream channel, μm
Q	flow rate, $\mu\text{l} \cdot \text{h}^{-1}$
q	flow rate ratio of oil and water ($=Q_o/Q_w$)
R_{drop}	droplet radius, μm
Re	Reynolds number ($=2\rho_o V_o R_{\text{drop}}/\mu_o$)
R_{jet}	thread radius, μm
Δt	time step size in VOF simulation, s
u_o	oil velocity distribution in orifice region, $\text{m} \cdot \text{s}^{-1}$
V_o	average velocity of oil in orifice region, $\text{m} \cdot \text{s}^{-1}$
\bar{V}	average slip velocity of the oil–water interface, $\text{m} \cdot \text{s}^{-1}$
v_{fluid}	maximum fluid velocity in VOF simulation, $\text{m} \cdot \text{s}^{-1}$
w	width of orifice, μm
w_{down}	width of the downstream channel, μm
Δx	grid size in VOF simulation, μm
α	volume fraction of water phase
β	constant referring to the shape factors in the modification of viscous drag
λ	viscosity ratio of oil and water ($=\mu_o/\mu_w$)
μ	viscosity, $\text{Pa} \cdot \text{s}$
ρ	density, $\text{kg} \cdot \text{m}^{-3}$
σ	interfacial tension coefficient, $\text{N} \cdot \text{m}^{-1}$

Subscripts

o	oil
w	water

Appendix

In the simplest 2D case, the microchannel is taken as a planar structure when the dimension in the thickness direction is far less than the other two, and the typical parallel flow holds. In the following, the velocity distribution of oil and water is derived, and the fact that the penetration of water will lead to the increase of oil pressure gradient is validated.

Since the Reynolds number is extremely low in this microfluidics and the stratified flow is nearly steady in the orifice, the Navier–Stokes equation can be simplified as the Stokes equation. As illustrated in Fig. A1, both the velocity profile is parabolic and only about y due to the assumptions of steady, laminar and fully developed flow. Non-slip boundary condition is considered near the

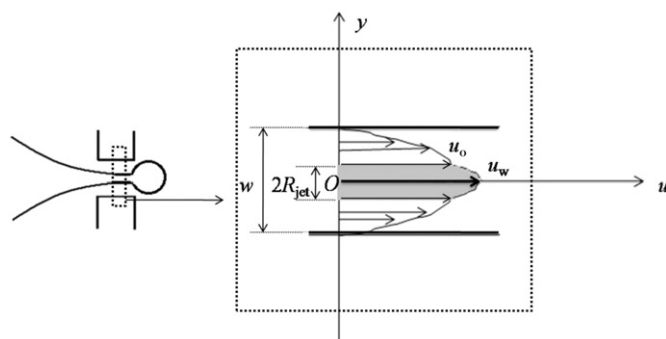


Fig. A1. Parabolic velocity profile of oil and water flow in orifice region.

channel wall, and zero shear stress must be satisfied within water phase at $y = 0$. Across the water–oil interface ($y = \pm R_{\text{jet}}$), the velocity u and shear stress τ of two liquid must be continuous, so the equation is written as

$$\begin{cases} \mu_{o,w} \left(\frac{d^2 u}{dy^2} \right)_{o,w} = \left(\frac{dp}{dx} \right)_{o,w} = \text{const} \\ u_o|_{y=\pm \frac{w}{2}} = 0, u_o|_{y=\pm R_{\text{jet}}} = u_w|_{y=\pm R_{\text{jet}}} \\ \left(\tau = \mu \frac{du}{dy} \right)_w|_{y=0} = 0 \\ \left(\tau = \mu \frac{du}{dy} \right)_o|_{y=\pm R_{\text{jet}}} = \left(\tau = \mu \frac{du}{dy} \right)_w|_{y=\pm R_{\text{jet}}} \end{cases} \quad (\text{A1})$$

from above we obtain the velocity profile as

$$u_o(y) = \frac{1}{2\mu_o} \left(\frac{dp}{dx} \right)_o \left[y^2 - \left(\frac{w}{2} \right)^2 \right] \quad (\text{A2})$$

$$u_w(y) = \frac{1}{2\mu_w} \left(\frac{dp}{dx} \right)_w (y^2 - R_{\text{jet}}^2) + \frac{1}{2\mu_o} \left(\frac{dp}{dx} \right)_o \left[R_{\text{jet}}^2 - \left(\frac{w}{2} \right)^2 \right]. \quad (\text{A3})$$

Two conclusions can be drawn from the above and extended to 3D flow case. First, we note that the expression of oil velocity distribution is the same in form as the traditional inner flow of single fluid between parallel plates. It suggests that the central penetration of water does not influence the form of oil velocity profile. However, it will cause an increase of oil pressure gradient to reach mass conservation of oil when the inlet flow rate is unaltered. Second, the velocity of water phase consists of the traditional parallel flow velocity and the slip velocity of water–oil interface.

References

- [1] W. Wang, R. Xie, X.J. Ju, T. Luo, L. Liu, D.A. Weitz, L.Y. Chu, Controllable microfluidic production of multicomponent multiple emulsions, *Lab Chip* 11 (9) (2011) 1587–1592.
- [2] A.D. Griffiths, D.S. Tawfik, Miniaturising the laboratory in emulsion droplets, *Trends Biotechnol.* 24 (9) (2006) 395–402.
- [3] Y. Schaerli, R.C. Wootton, T. Robinson, V. Stein, C. Dunsby, M.A.A. Neil, P.M.W. French, A.J. Demello, C. Abell, F. Hollfelder, Continuous-flow polymerase chain reaction of single-copy DNA in microfluidic microdroplets, *Anal. Chem.* 81 (1) (2009) 302–306.
- [4] Z. Zhu, G. Jenkins, W.H. Zhang, M.X. Zhang, Z.C. Guan, C.Y.J. Yang, Single-molecule emulsion PCR in microfluidic droplets, *Anal. Bioanal. Chem.* 403 (8) (2012) 2127–2143.
- [5] M. Nakano, J. Komatsu, S. Matsuura, K. Takashima, S. Katsura, A. Mizuno, Single-molecule PCR using water-in-oil emulsion, *J. Biotechnol.* 102 (2) (2003) 117–124.
- [6] K. Tang, A. Gomez, Generation by electrospray of monodisperse water droplets for targeted drug-delivery by inhalation, *J. Aerosol Sci.* 25 (6) (1994) 1237–1249.
- [7] Z.Z. Wong, J.L. Bull, Vascular bubbles and droplets for drug delivery, *J. Drug Deliv. Sci. Tec.* 21 (5) (2011) 355–367.
- [8] G.G. Su, P.W. Longest, R.M. Pidaparti, novel micropump droplet generator for aerosol drug delivery: design simulations, *Biomicrofluidics* 4 (4) (2012) 044108.
- [9] H.C. Shum, A. Bandyopadhyay, S. Bose, D.A. Weitz, Double emulsion droplets as microreactors for synthesis of mesoporous hydroxyapatite, *Chem. Mater.* 21 (22) (2009) 5548–5555.
- [10] L.M. Fidalgo, G. Whyte, B.T. Ruotolo, J.L.P. Benesch, F.C. Stengel, C. Abell, C.V. Robinson, W.T. Huck, Coupling microdroplet microreactors with mass spectrometry: reading the contents of single droplets online, *Angew. Chem. Int. Ed.* 48 (20) (2009) 3665–3668.
- [11] P. Garstecki, I. Gitlin, W. DiLuzio, G.M. Whitesides, E. Kumacheva, H.A. Stone, Formation of monodisperse bubbles in a microfluidic flow-focusing device, *Appl. Phys. Lett.* 85 (13) (2004) 2649–2651.
- [12] L. Yobas, S. Martens, W.L. Ong, N. Ranganathan, High-performance flow-focusing geometry for spontaneous generation of monodispersed droplets, *Lab Chip* 6 (8) (2006) 1073–1079.
- [13] M. Seo, C. Paquet, Z. Nie, S. Xu, E. Kumacheva, Microfluidic consecutive flow-focusing droplet generators, *Soft Matter* 3 (8) (2007) 986–992.
- [14] S. Takeuchi, P. Garstecki, D.B. Weibel, G.M. Whitesides, An axisymmetric flow-focusing microfluidic device, *Adv. Mater.* 17 (8) (2005) 1067–1072.
- [15] S.L. Anna, N. Bontoux, H.A. Stone, Formation of dispersions using “flow focusing” in microchannels, *Appl. Phys. Lett.* 82 (3) (2003) 364–366.
- [16] A.S. Utada, E. Lorenceau, D.R. Link, P.D. Kaplan, H.A. Stone, D.A. Weitz, Monodisperse double emulsions generated from a microcapillary device, *Science* 308 (5721) (2005) 537–541.
- [17] H.W. Shao, Y.C. Lu, K. Wang, G.S. Luo, An experimental study of liquid–liquid microflow pattern maps accompanied with mass transfer, *Chin. J. Chem. Eng.* 20 (1) (2012) 18–26.
- [18] Y. Morimoto, W.H. Tan, S. Takeuchi, Three-dimensional axisymmetric flow-focusing device using stereolithography, *Biomed. Microdevices* 11 (2) (2008) 369–377.
- [19] M.W. Weber, R. Shandas, Computational fluid dynamics analysis of microbubble formation in microfluidic flow-focusing devices, *Microfluid. Nanofluid.* 3 (2) (2006) 195–206.
- [20] X.G. Zhang, Dynamics of drop formation in viscous flows, *Chem. Eng. Sci.* 12 (1999) 1759–1774.
- [21] Z. Nie, M. Seo, S. Xu, P.C. Lewis, M. Mok, E. Kumacheva, G.M. Whitesides, P. Garstecki, H.A. Stone, Emulsification in a microfluidic flow-focusing device: effect of the viscosities of the liquids, *Microfluid. Nanofluid.* 5 (5) (2008) 585–594.
- [22] P. Garstecki, H.A. Stone, G.M. Whitesides, Mechanism for flow-rate controlled breakup in confined geometries: A route to monodisperse emulsions, *Phys. Rev. Lett.* 94 (16) (2005) 164501.
- [23] B. Dollet, W. Hoeve, J.P. Raven, P. Marmottant, M. Versluis, Role of the channel geometry on the bubble pinch-off in flow-focusing devices, *Phys. Rev. Lett.* 100 (3) (2008) 034504.
- [24] X.G. Zhang, Dynamics of growth and breakup of viscous pendant drops into air, *J. Colloid Interface Sci.* 212 (1) (1999) 107–122.
- [25] G.F. Christopher, S.L. Anna, Microfluidic methods for generating continuous droplet streams, *J. Phys. D: Appl. Phys.* 40 (19) (2007) R319–R336.
- [26] M.R. Davidson, D.J.E. Harvie, J.J. Cooper-White, Flow focusing in microchannels, *ANZIAM J.* 46 (2005) 47–58 E.
- [27] A. Utada, A. Fernandez-Nieves, H.A. Stone, D.A. Weitz, Dripping to jetting transitions in coflowing liquid streams, *Phys. Rev. Lett.* 99 (9) (2007) 094502.
- [28] H. Lamb, On the uniform motion of a sphere through a viscous fluid, *Phil. Mag.* 21 (121) (1911) 112–121.
- [29] H. Brenner, Effect of finite boundaries on the stokes resistance of an arbitrary particle, *J. Fluid Mech.* 12 (1) (1962) 35–48.
- [30] J. Xu, G. Luo, G. Chen, J. Wang, Experimental and theoretical approaches on droplet formation from a micrometer screen hole, *J. Membr. Sci.* 266 (1–2) (2005) 121–131.
- [31] F. White, *Viscous Fluid Flow*, McGraw-Hill, New York, 1974.
- [32] A. Chandorkar, S. Palit, Simulation of droplet-based microfluidics devices using a volume of fluid (VOF) approach, in: M. Laudon, B. Romanowicz (Eds.), Technical Proceedings of Conference & Expo 2009, Vol.3, 2009, pp. 396–400 (Houston).
- [33] A. Theodorakakos, G. Bergeles, Simulation of sharp gas–liquid interface using VOF method and adaptive grid local refinement around the interface, *Int. J. Numer. Methods Fluids* 45 (4) (2004) 421–439.
- [34] S. Hardt, An extended volume-of-fluid method for micro flows with short-range interactions between fluid interfaces, *Phys. Fluids* 17 (10) (2005) 100601.
- [35] R.Y. Hong, Numerical study of pinching liquid filament using VOF method, *Chin. J. Chem. Eng.* 11 (5) (2003) 542–549.
- [36] X.B. Zhang, L. Yao, L.M. Qiu, X.J. Zhang, Three-dimensional computational fluid dynamics modeling of two-phase flow in a structured packing column, *Chin. J. Chem. Eng.* 21 (9) (2013) 959–966.
- [37] J.U. Brackbill, D.B. Kothe, C. Zemach, A continuum method for modelling surface tension, *J. Comput. Phys.* 100 (2) (1992) 335–354.
- [38] W.Y. Fan, X.H. Yin, Numerical study on interaction between two bubbles rising side by side in CMC solution, *Chin. J. Chem. Eng.* 21 (7) (2013) 705–713.
- [39] J.C. McDonald, G.M. Whitesides, Poly(dimethylsiloxane) as a material for fabricating microfluidic devices, *Acc. Chem. Res.* 35 (7) (2002) 491–499.